

Molecular switches regulating the potency and immune evasiveness of SARS-CoV-2 spike protein

Yushun Wan

University of Minnesota

Linfen Huang

University of Minnesota

Xiujuan Zhang

Lindsley F. Kimball Research Institute

Jian Shang

University of Minnesota

Stanley Perlman

University of Iowa

Lanying Du

Lindsley F. Kimball Research Institute

Fang Li (✉ lifang@umn.edu)

University of Minnesota

Research Article

Keywords: SARS-CoV-2, spike protein, receptor-binding domain, ACE2 binding, viral entry, immune evasiveness, cryo-EM structures

Posted Date: July 21st, 2021

DOI: <https://doi.org/10.21203/rs.3.rs-736159/v1>

License:  This work is licensed under a Creative Commons Attribution 4.0 International License.

[Read Full License](#)

1
2
3
4
5
6
7
8
9
10
11
12
13
14
15
16
17
18
19
20
21
22
23
24
25
26

**Molecular switches regulating the potency and immune evasiveness
of SARS-CoV-2 spike protein**

Yushun Wan ^{1,2}, Linfen Huang ^{1,2}, Xiujuan Zhang ³, Jian Shang ^{1,2},
Stanley Perlman ⁴, Lanying Du ³, Fang Li ^{1,2}#

¹ Department of Veterinary and Biomedical Sciences, University of Minnesota, Saint Paul, MN, USA

² Center for Coronavirus Research, University of Minnesota, Saint Paul, MN, USA

³ Laboratory of Viral Immunology, Lindsley F. Kimball Research Institute, New York Blood Center, New York, NY, USA

⁴ Department of Microbiology and Immunology, University of Iowa, Iowa City, IA, USA

Correspondence:

Fang Li (lifang@umn.edu)

Keywords: SARS-CoV-2, spike protein, receptor-binding domain, ACE2 binding, viral entry, immune evasiveness, cryo-EM structures

Running title: Dynamics between potency and evasiveness of SARS-CoV-2

27 **Abstract**

28 What enabled SARS-CoV-2, but not other coronaviruses, to cause a global
29 pandemic? Here we investigated key structural determinants of the pandemic. Using
30 SARS-CoV-1 and bat RaTG13-CoV as comparisons, we identified two molecular
31 switches that regulate the conformations of SARS-CoV-2 spike protein: (i) a furin motif
32 loop turns SARS-CoV-2 spike from a closed conformation to a mixture of open and
33 closed conformations, and (ii) a K417V mutation turns SARS-CoV-2 spike from mixed
34 conformations to an open conformation. We showed that the open conformation favors
35 viral potency by exposing the RBD for receptor binding and viral entry, while the closed
36 conformation supports viral immune evasion by hiding the RBD from neutralizing
37 antibodies. Hence SARS-CoV-2 spike has evolved to reach a balance between potency
38 and immune evasiveness, which contributes to the pandemic spread of SARS-CoV-2.
39 The dynamics between viral potency and invasiveness is likely to further evolve,
40 providing insights into future evolution of SARS-CoV-2.

41

42

43 **Introduction**

44 Coronaviruses have a long history of infecting humans and animals, yet none had
45 caused the same devastation as produced by SARS-CoV-2^{1,2}. For example, a virulent
46 and lethal coronavirus, SARS-CoV-1, yielded a much smaller outbreak in humans in
47 2002-2003^{3,4}. Numerous human coronaviruses such as NL63-CoV cause common colds
48 annually^{5,6}. With an intermediate virulence, SARS-CoV-2 causes a fatality rate that is
49 significantly lower than that of SARS-CoV-1, but much higher than that of NL63-CoV.
50 SARS-CoV-2 carriers show clinical signs that facilitate the spread of the virus: they may
51 develop mild or no symptoms, experience delayed onset of symptoms, develop low levels
52 of neutralizing antibodies, or endure prolonged virus shedding period⁷⁻¹¹. These features
53 contribute to the wide spread of SARS-CoV-2 and severe health outcomes, triggering a
54 global COVID-19 pandemic that is unprecedented in the era of modern medicine. What
55 are the molecular determinants of these clinical features of COVID-19? This study aims
56 to address this question at the molecular and structural levels.

57 Understanding the molecular determinants of COVID-19 provides important clues
58 to the evolution and cross-species transmission of coronaviruses. A dangerous feature of
59 coronaviruses is their propensity to cross species barriers^{12,13}. In fact, coronaviruses
60 similar to human coronaviruses such as SARS-CoV-1 and NL63-CoV have been
61 identified in bats and other animals¹⁴⁻¹⁶. RaTG13-CoV, a coronavirus with ~96%
62 genomic sequence homology with SARS-CoV-2, has been identified in bats¹⁷. Thus,
63 coronaviruses that originate from bats or other animals pose a long-term threat to
64 humans. A comparison of the molecular mechanisms of SARS-CoV-2 and other
65 coronaviruses not only facilitate an understanding of the COVID-19 pandemic, but also

66 shed light on the evolution of coronaviruses, including their cross-species transmission
67 and adaptation to humans.

68 The viral-envelope-anchored spike protein guides coronavirus entry into host cells
69 ¹⁸. At the same time, it is a major target for the host immune responses ¹⁹. On newly
70 packaged virus particles, the trimeric spike protein has a pre-fusion structure in which
71 three receptor-binding S1 subunits sit on top of a trimeric membrane-fusion S2 stalk (Fig.
72 1A, 1B). During viral entry, a receptor-binding domain (RBD) in S1 binds to a receptor
73 on host cell surface for viral attachment ²⁰; subsequently S1 dissociates and S2 switches
74 to a post-fusion structure for the fusion of viral and host membranes ¹⁸. For the pre- to
75 post-fusion structural change to take place, all coronavirus spikes need to be cleaved by
76 host proteases ^{21,22}. SARS-CoV-2, SARS-CoV-1, NL63-CoV and RaTG13-CoV can all
77 use ACE2 as the receptor ^{17,23-26}, but SARS-CoV-2 spike contains two unique features.
78 First, only SARS-CoV-2 spike contains a furin motif at the S1/S2 boundary ²⁷, which
79 allows SARS-CoV-2 spike to be pre-activated by furin from previously infected cells.
80 Second, the pre-fusion structure of SARS-CoV-2 is present in two conformations with
81 approximately equal ratio: an open conformation in which the RBD is exposed and
82 accessible to ACE2 and a closed conformation in which the RBD is buried and
83 inaccessible to ACE2 ^{28,29}. In contrast, SARS-CoV-1 spike is mainly open and NL63-
84 CoV and RaTG13-CoV spikes are only closed ³⁰⁻³². Yet despite the extensive structural
85 studies of coronavirus spikes (Table S1), it is unclear what molecular switches regulate
86 their conformations or how the conformational changes affect viral functions and host
87 immune responses.

88 Here we compared the spike proteins of the three ACE2-recognizing
89 coronaviruses. Using biochemical, pseudovirus, cryo-EM, and animal immunization
90 assays, we first identified the molecular switches that regulate the RBD conformations in
91 SARS-CoV-2 spike. We then demonstrated that whereas the open conformation of
92 SARS-CoV-2 spike increases its potency, the closed conformation allows it to evade host
93 immune responses. Through regulation of its spike's conformations, SARS-CoV-2 may
94 have struck a balance between viral potency and evasiveness. The dynamics of this
95 balance may further evolve, shedding light on future evolution of SARS-CoV-2.

96

97 **Results**

98 To understand the molecular mechanisms that control the spike RBD switching
99 between open and closed conformations, we conducted a comparative study of SARS-
100 CoV-2 and the other ACE2-recognizing coronaviruses. Sequence analysis showed that
101 compared to the closely related SARS-CoV-1 and RaTG13-CoV, only SARS-CoV-2
102 spike contains a four-residue PRRA insertion ahead of a conserved Arg685 at the S1/S2
103 junction, constituting the furin motif (FnM) (Fig. 1A, 1B). Hence we introduced
104 mutations to inactivate the FnM in SARS-CoV-2 spike in three ways: (i) point mutations
105 from PRRA to PAGA (i.e., FnM-point); (ii) deletion mutation based on SARS-CoV-1
106 spike (i.e., FnM-deletion); (iii) deletion mutation based on RaTG13-CoV (i.e., FnM-
107 deletion-2). We then explored whether these FnM mutations affected the conformation
108 and potency of SARS-CoV-2 spike.

109 To this end, we characterized the capabilities of the FnM mutant spikes of SARS-
110 CoV-2 in binding human ACE2 and mediating viral entry. First, we expressed the wild

111 type and mutant spikes on cell surface (Fig. 1C). The result showed that during the
112 maturation process, a significant amount of wild type spike molecules had been cleaved
113 by furin. In contrast, none of the three types of FnM mutant spikes had undergone
114 significant cleavage, suggesting that inactivation of FnM successfully suppressed furin
115 cleavage of the spikes. Second, we performed a protein pull-down assay using
116 recombinant human ACE2 as the bait and the cell-surface-anchored spikes as the target.
117 For cross validation, both His-tagged ACE2 and Fc-tagged ACE2 were used. We
118 previously showed that this pull-down assay is a reliable method to probe the RBD
119 conformation in cell-surface-anchored spikes, with higher pull-down levels of the spikes
120 associated with more spike molecules in the RBD-open conformation²⁷. Our results
121 showed that the wild type and FnM-point spikes had similar affinities for ACE2, and both
122 demonstrated much higher affinities for ACE2 than the two FnM-deletion spikes (Fig.
123 1C). Third, we performed a pseudovirus entry assay where retroviruses pseudotyped with
124 SARS-CoV-2 spike (i.e., SARS-CoV-2 pseudoviruses) were used to enter cells
125 expressing human ACE2 (Fig. 1D). The result showed that the FnM-point spikes
126 mediated pseudovirus entry slightly worse than the wild type spike, suggesting that furin
127 pre-activation had small, albeit significant, impact on SARS-CoV-2 spike's capability in
128 mediating viral entry. In contrast, both of the FnM-deletion spikes mediated pseudovirus
129 entry much worse than both the wild type spike and FnM-point spike, suggesting that the
130 closed conformation of the spike substantially reduced its capability to mediate viral
131 entry. The data from protein pull-down and pseudovirus entry assays revealed that FnM
132 deletion resulted in decreased potency of SARS-CoV-2 spike, as demonstrated in reduced
133 ACE2 binding and reduced capability of mediating viral entry. These results suggest that

134 due to the FnM deletion, more SARS-CoV-2 spike molecules switched to the closed
135 conformation with reduced potency.

136 Next we directly visualized the conformation of SARS-CoV-2 spike containing
137 the FnM deletion using cryo-EM. To this end, we expressed and purified the ectodomain
138 of SARS-CoV-2 spike containing the FnM deletion (it also contained a C-terminal foldon
139 trimerization tag and two proline mutations in S2, both of which stabilize the pre-fusion
140 structure). As a comparison, we also prepared the ectodomain of SARS-CoV-2 spike
141 containing the FnM point mutation (in addition to the foldon tag and proline mutations).
142 We then collected cryo-EM data on both of these proteins and performed 3-D
143 classifications of the particles based on their conformations (Fig. 2A, 2B; Fig. S1). Our
144 results showed that 48% of FnM-point spike molecules are in the open conformation with
145 one of the three RBDs exposed and the 52% of the molecules were in the closed
146 conformation with all three RBDs hidden (Fig. 2B). This result is consistent with two
147 previous studies showing an approximately equal ratio of open and closed spike
148 molecules (one of the studies involved recombinant FnM-point spike ectodomain and the
149 other virus-surface wild type full-length spike)^{28,29}. In contrast, our cryo-EM result
150 showed that all of the FnM-deletion spike molecules were in the closed conformation
151 with all three RBDs hidden (Fig. 2A). Therefore, consistent with our biochemical data,
152 our cryo-EM data confirmed that the FnM deletion caused SARS-CoV-2 spike to switch
153 to the closed conformation.

154 We further determined the cryo-EM structures of SARS-CoV-2 FnM-deletion
155 spike ectodomain at 3.8 Å and FnM-point spike ectodomain at 4.4 Å (Fig. 2A, 2B; Fig.
156 S2A, Fig. S2B). Overall, the two structures are similar to each other and to the previously

157 determined cryo-EM structures of FnM-point spike ectodomain and virus-surface wild
158 type full-length spike^{28,29}. In the trimeric spike structures, each S1 subunit contains an N-
159 terminal domain (NTD), an RBD, and two subdomains (SD1 and SD2); the RBD from
160 one S1 subunit packs against the NTD from another S1 subunit and it also packs against
161 the two RBDs from the other two S1 subunits (Fig. S3A)²⁸. Moreover, the RBD switches
162 between the open and closed conformations by rotating around a hinge region connecting
163 SD1 and SD2; SD2, which harbors the FnM loop, directly interacts with the hinge region
164 and the NTD (Fig. S3A)²⁸. Detailed structural analysis revealed that compared to the
165 FnM-point spike, the RBD and NTD in each S1 subunit of the FnM-deletion spike
166 rotated towards each other by $\sim 2.5^\circ$ (Fig. S4A). Because of this movement, compared to
167 the FnM-point spike, the RBD/NTD interface, the RBD/RBD interface and hence the
168 total interface in trimeric S1 all increased significantly in the FnM-deletion spike, leading
169 to enhanced S1 packing (Fig. S3B). As a comparison, the corresponding interfaces in a
170 previously determined FnM-point spike were similar to those in our FnM-point spike
171 (Fig. S3B)²⁸. What caused this structural change is not obvious due to the lack of density
172 in the FnM loop and another loop (i.e., anchor loop) in SD2 from all the available
173 structures of SARS-CoV-2 spike. However, the structures of the FnM loop and the
174 anchor loop were resolved in the mouse hepatitis coronavirus (MHV) spike structure that
175 we recently determined³³. Because the MHV and SARS-CoV-2 spikes have overall
176 similar structures (Fig. S4B), we combined the structural information from these two
177 spikes, which revealed an interaction network involving the FnM loop, anchor loop, the
178 hinge region, and the NTD (Fig. S4B). Hence, one possibility is that the FnM deletion
179 disturbed this interaction network and caused the movements of the RBD and NTD,

180 which subsequently led to enhanced S1 packing, reduced dynamics of the RBD and
181 hence the closed spike. Thus, as supported by the biochemical data and 3D classification
182 data, the physical presence of the FnM, instead of furin cleavage per se, leads to open
183 spike molecules by reducing S1 packing.

184 To further understand the relationship between the presence of FnM and the
185 conformation of the spikes, we inserted FnM into RaTG13-CoV spike (i.e., FnM-insert)
186 (Fig. 3A). As a comparison, we also inserted a random sequence, glycine-serine-glycine-
187 serine, into the same location as the inserted FnM in RaTG13-CoV spike (i.e., GSGS-
188 insert) (Fig. 3A). When expressed on cell surfaces, FnM-insert spike, but not wild type
189 spike or GSGS-insert spike, was cleaved by furin (Fig. 3B), confirming the introduction
190 of FnM. We could not obtain recombinant RaTG13 spike ectodomains (wild type or
191 mutants) that were stable enough for cryo-EM analysis (recombinant spike ectodomains
192 are generally less stable than full-length membrane-anchored spikes). Instead, we
193 examined the RBD conformations of the mutant spikes using protein pull-down and
194 pseudovirus entry assays (Fig. 3B, 3C). Compared to the wild type spike, both the FnM-
195 insert and FnM-GSGS RaTG13-CoV spikes bound to human ACE2 with higher affinity
196 and mediated pseudovirus entry more efficiently. Thus, the physical presence of FnM or
197 another random sequence in the FnM loop opens up RaTG13-CoV spike and enhances its
198 potency.

199 Having identified the FnM loop as a key determinant for the conformation of
200 SARS-CoV-2 spike, we asked why SARS-CoV-1 spike is in the open conformation
201 despite its lack of FnM. To address this question, we compared the sequences of SARS-
202 CoV-2 and SARS-CoV-1 spikes in the context of their tertiary structures. We identified

203 residue 417 as potentially a key difference between the two spikes: in the closed SARS-
204 CoV-2 spike, Lys417 in the RBD forms a salt bridge with the RBD from another subunit,
205 stabilizing the RBD in the closed conformation and hence enhancing S1 packing; it
206 becomes a valine in SARS-CoV-1 spike, losing its capability to interact with the other
207 subunit and hence reducing S1 packing (Fig. 4A). We introduced the K417V mutation
208 into SARS-CoV-2 spike, and examined its impact on the conformation of SARS-CoV-2
209 spike. Both the protein pull-down and pseudovirus entry assays demonstrated that
210 compared to the wild type spike, the K417V mutation allowed more spike molecules to
211 open up for binding ACE2 and mediating viral entry (Fig. 4B, 4C). We could not obtain
212 recombinant SARS-CoV-2 K417V spike ectodomain that was stable enough for cryo-EM
213 analysis. Instead, we prepared recombinant SARS-CoV-2 spike ectodomain containing
214 the K417V mutation and FnM deletion (in addition to proline mutations) (K417V/FnM-
215 deletion). Cryo-EM analysis at 4.6 Å revealed that 91% of the K417V/FnM-deletion
216 spike molecules were open and 9% were closed (Fig. 2C). In comparison, as presented
217 earlier, 100% of the recombinant FnM-deletion spike molecules were closed (Fig. 2A).
218 Therefore, despite lacking FnM, SARS-CoV-1 spike is open due to Val417 and
219 potentially other residues that destabilize the closed conformation of the RBD and reduce
220 S1 packing.

221 To understand how the RBD conformations of SARS-CoV-2 spike affect host
222 immune responses targeting the RBD, we immunized mice with one of the following
223 three recombinant SARS-CoV-2 spike ectodomains: FnM-deletion spike, FnM-point
224 spike, and K417V/FnM-deletion spike (in addition to the proline mutations in all of
225 them). Four weeks after the initial immunization, the mice were further boosted with the

226 same immunogen. Ten days after the second immunization, mouse sera were collected.
227 We measured the amounts of RBD-specific antibodies in the mouse sera using ELISA.
228 The result showed that K417V/FnM-deletion spike and FnM-point spike induced
229 significantly more RBD-specific antibodies than FnM-deletion spike (Fig. 5A). We
230 further measured the amounts of neutralizing antibodies in the mouse sera using
231 pseudovirus entry inhibition assay. The result showed that K417V/FnM-deletion spike
232 and FnM-point spike induced significantly more neutralizing antibodies than FnM-
233 deletion spike (Fig. 5B). These data confirm that more molecules of K417V/FnM-
234 deletion spike and of FnM-point spike are in the open conformations than FnM-deletion
235 spike. They also reveal that compared to open spikes, closed spikes trigger lower levels
236 of RBD-targeting antibodies and neutralizing antibodies and hence their RBDs and spikes
237 are more evasive to the host immune system.

238 To summarize, we investigated the molecular switches regulating the
239 conformation of SARS-CoV-2 spike protein. We used four different experimental
240 approaches: pull-down of cell-surface spikes, cryo-EM analysis of recombinant spike
241 ectodomains, spike-mediated pseudovirus entry, and immunization of mice with
242 recombinant spike ectodomains. To date, several other studies also investigated the
243 conformations of SARS-CoV-2 spike using cryo-EM^{28,29,31,34,35}, some of which gave
244 different ratios of open and closed spikes probably due to differences in sample
245 preparations and/or protein constructions. The ratio of open and closed spikes in our
246 FnM-point construct is similar to two other studies: a study that examined the full-length
247 virus-anchored SARS-CoV-2 spike (which is likely the most physiologically relevant)²⁹
248 and another study that used the same protein construct and similar protein preparation to

249 the current study ²⁸. Importantly, our cryo-EM analysis of a variety of SARS-CoV-2
250 mutant spike ectodomains is consistent with our three other experimental approaches.
251 Overall, in terms of experimental approaches, the current study is among the most
252 comprehensive ones in investigating the conformation of SARS-CoV-2 spike; in terms of
253 conceptual advances, the current study is the first to investigate molecular switches
254 regulating the conformations of SARS-CoV-2 spike.

255

256 **Discussion**

257 What molecular features of SARS-CoV-2 set the virus apart from other
258 coronaviruses and triggered the COVID-19 pandemic? Three prominent features
259 characterize SARS-CoV-2 spike: high ACE2-binding affinity of the RBD, the presence
260 of the furin motif at the S1/S2 boundary, and the RBD switching between open and
261 closed conformations ²⁶⁻²⁸. Among these features, the molecular mechanisms for the first
262 two have been well established in previous research on SARS-CoV-1 and MERS-CoV
263 (MERS-CoV spike contains a furin motif) ^{18,20,36}. These two features facilitated SARS-
264 CoV-1 and MERS-CoV, respectively, to infect humans, yet neither virus caused a
265 pandemic. Here we showed that a unique determinant of the COVID-19 pandemic resides
266 in the molecular mechanisms of the conformations of SARS-CoV-2 spike. To our
267 knowledge, this study is the first to show that the conformations of coronavirus spike
268 proteins are regulated through one or a few molecular and structural switches. It is also
269 the first to provide direct evidence on the functions of these conformational changes of
270 coronavirus spikes. It has important implications for the structure, function and evolution
271 of coronavirus spikes and for the current and potentially future coronavirus infections.

272 How do the conformations of SARS-CoV-2 spike impact viral entry and host
273 immune responses? Among the coronavirus spikes whose tertiary structures are available,
274 only three showed a significant presence of open conformations in cryo-EM studies:
275 those from SARS-CoV-2, SARS-CoV-1, and MERS-CoV (Table S1). All three are novel
276 coronaviruses that recently infected humans. In contrast, coronaviruses with closed spikes
277 all have established infections in their respective hosts (the spikes would need to open
278 briefly for receptor binding). This difference suggests that the open spike facilitates novel
279 coronaviruses to infect humans. Consistent with this hypothesis, here we showed that
280 compared to closed spikes, open spikes mediate more efficient receptor binding and viral
281 entry. An open conformation, however, did not trigger a pandemic from SARS-CoV-1 or
282 MERS-CoV, neither does it explain why established coronaviruses all have closed spikes.
283 What makes SARS-CoV-2 spike unique is a balanced ratio between open and closed
284 conformations, which may enhance immune evasion during its transmission in humans.
285 Consistent with this hypothesis, here we showed that more spike molecules in the closed
286 conformation correspond to decreased inductions of RBD-targeting antibodies and
287 neutralizing antibodies in mice. Together, these findings demonstrate that the presence of
288 open and closed conformations of its spike allows SARS-CoV-2 to balance its potency
289 and immune evasiveness.

290 How has SARS-CoV-2 spike evolved to reach the balance of potency and
291 evasiveness? Through comparative studies of the spikes from SARS-CoV-2, SARS-CoV-
292 1 and RaTG13-CoV, we identified two molecular switches for the open and closed
293 conformational changes of SARS-CoV-2 spike: the physical presence of the furin motif
294 loop and the mutation of residue 417, both of which regulate S1 packing. Thus, one or

295 several structural changes in coronavirus spikes can function as molecular switches for
296 the conformations of coronavirus spikes. Other molecular determinants may also exist to
297 control the opening and closing of coronavirus spikes, but these two naturally occurring
298 molecular determinants help understand the evolution of coronavirus spikes.
299 Coronaviruses that have evolved molecular switches to open up their spike have an
300 advantage in spreading efficiently in the infected host species. In contrast, those that have
301 evolved mechanisms to close down their spikes have an advantage in establishing evasive
302 and long-lasting infections in the infected host species.

303 These findings lead us to propose the following molecular mechanisms for the
304 COVID-19 pandemic. First, adaptation of SARS-CoV-2 RBD to human ACE2 and furin
305 cleavage of SARS-CoV-2 spike both play important roles in the transmission of SARS-
306 CoV-2 in humans. Second, a balanced open and closed RBD conformations of SARS-
307 CoV-2 spike enable the virus to be both potent and immune evasive. Unlike the stepwise
308 accumulation of point mutations in the RBD for enhanced ACE2 binding, the molecular
309 switches for the RBD conformations of the spike allow more drastic and efficient control
310 of ACE2 binding and viral entry. The opening up of its spike likely facilitates SARS-
311 CoV-2 to gain infection potency and spread efficiently in humans. With an open spike,
312 SARS-CoV-1 and MERS-CoV are virulent and lethal, but they are also immune exposed.
313 These features of the two viruses contributed to the short incubation time, easy-to-detect
314 symptoms and relatively quick recovery of patients, allowing the viruses to be contained
315 by human interventions (e.g., quarantine) and immune systems. In contrast, with balanced
316 conformations of its spike, SARS-CoV-2 is less virulent but more immune evasive. This
317 feature of SARS-CoV-2 contributes to the relatively long incubation time, harder-to-

318 detect symptoms (even asymptomatic infections), low neutralizing antibodies, or long
319 virus shedding period in patients; these clinical symptoms of patients further contribute to
320 the wide spread of SARS-CoV-2. Therefore, the balanced potency and immune
321 evasiveness of SARS-CoV-2 spike contributes to the wide spread of SARS-CoV-2.

322 Our findings also provide insights into how SARS-CoV-2 may further evolve.
323 When SARS-CoV-2 first entered humans, it spread unchecked due to little immune
324 resistance. The more open and potent spike gave the virus an advantage in spreading
325 widely. Several months in the pandemic, a D614G mutation allowed more SARS-CoV-2
326 spike molecules to open up^{37,38}, a sign that the virus was gaining more potency³⁹.
327 However, as infection cases rise and vaccinations get underway, SARS-CoV-2 is likely to
328 evolve towards better immune evasiveness eventually. This may happen through an
329 increase in the proportion of closed spikes, making the virus more immune evasive but
330 less potent. If that happens, SARS-CoV-2 may become an endemic (but milder) virus like
331 NL63-CoV (NL63-CoV RBD binds to human ACE2 with high affinity, but is hidden in
332 the closed spike)^{25,30,40}. This study showed that just one or a few structural changes in the
333 spike protein can significantly impact the dynamics between viral potency and
334 evasiveness. This makes coronaviruses a current and future danger to human health.
335 Understanding the molecular determinants that regulate the potency and evasiveness of
336 coronaviruses is critical not only for our understanding the current COVID-19 pandemic,
337 but also for monitoring and preparing for potential future coronavirus pandemics.

338 **Acknowledgements**

339 This work was supported by NIH grants R01AI089728 and R01AI110700 (to
340 F.L.) and NIH grants R01AI139092 (to F.L. and L.D.). Cryo-EM data were collected at
341 the John M. Cowley Center for High Resolution Electron Microscopy of Arizona State
342 University and the Electron Microscopy facility of Purdue University. We thank Dewight
343 Williams, Wei Zhang and Thomas Klose for helping us prepare grids and collect cryo-
344 EM data. The cryo-EM maps and atomic models have been deposited in the Electron
345 Microscopy Data Bank (EMDB) and Protein Data Bank (PDB), respectively, under the
346 following accession codes: EMD-9409 (EMDB) and 5BKP (PDB) for FnM-deletion
347 SARS-CoV-2 spike and EMD-9408 (EMDB) and 5BKO (PDB) for FnM-point SARS-
348 CoV-2 spike. We thank Professor Kathryn Holmes for discussion and edits to the
349 manuscript.

350

351 **Materials and Methods**

352 *Plasmids*

353 All of the protein constructs in this study were cloned into pcDNA 3.1 vector
354 (Life Technologies). SARS-CoV-2 spike (GenBank accession number QHD43416.1),
355 SARS-CoV-1 spike (GenBank accession number YP_009825051.1), RaTG13-CoV spike
356 (GenBank accession number QHR63300.2), and human ACE2 (GenBank accession
357 number NM_021804) were all synthesized (GenScript Biotech) and cloned into the
358 vector containing a C-terminal c9 tag. SARS-CoV-2 spike ectodomains (residues 1-1211)
359 were cloned into the vector containing mutations of interest, in addition to two proline
360 mutations in S2 (K986P, V987P), a C-terminal foldon trimerization tag, and a C-terminal
361 His₆-tag. SARS-CoV-2 spike RBD (residues 319-535) and SARS-CoV-1 spike RBD
362 (residues 306-521) were cloned into the vector containing an N-terminal tPA signal
363 peptide. Human ACE2 ectodomain (residues 1–615) were cloned into the vector
364 containing either a C-terminal His₆-tag or Fc-tag.

365 *Protein expression and purification*

366 All of the recombinant proteins were expressed in 293F cells (Thermo Fisher)
367 using a FreeStyle 293 mammalian cell expression system (Life Technologies) as
368 previously described ⁴¹. In brief, the His-tagged proteins were collected from cell culture
369 medium, purified using a Ni-NTA column (Cytiva Healthcare), purified further using a
370 Superdex gel filtration column (Cytiva Healthcare), and stored in a buffer containing 20
371 mM Tris pH 7.4 and 200 mM NaCl. The Fc-tagged protein was purified in the same way
372 as the His-tagged proteins, except that the protein A column replaced the Ni-NTA
373 column in the procedure.

374 *Pseudovirus entry*

375 Pseudoviruses were packaged as previously described⁴². Briefly, pcDNA3.1(+)
376 plasmid encoding one of the full-length coronavirus spike genes (wild type or mutant)
377 was co-transfected into HEK293T cells with helper plasmid psPAX2 and reporter
378 plasmid plenti-CMV-luc at a molar ratio of 1:1:1 using Lipofectamine 3000 (Life
379 Technologies). The produced pseudoviruses were harvested 72 hours post transfection
380 and then were used to enter HEK293T cells expressing human ACE2. After incubation at
381 37°C for 5 hours, medium was replaced and cells were incubated for an additional 48
382 hours. Cells were then washed with PBS and lysed. Aliquots of cell lysates were
383 transferred to Optiplate-96 (PerkinElmer), followed by addition of luciferase substrate.
384 Relative light unites (RLUs) were measured using EnSpire plate reader (PerkinElmer). In
385 the meanwhile, the amounts of pseudovirus-packaged spikes were measured by western
386 blot using an anti-c9 antibody and then were quantified using Fiji (<https://imagej.net/>).
387 The RLUs were then normalized against the amounts of pseudovirus-packaged spikes.
388 All of the measurements were carried out in quadruplicates.

389 For pseudovirus entry inhibition, mouse sera were serially diluted in DMEM
390 media and then mixed with SARS-CoV-2 pseudoviruses. Subsequently the mixtures were
391 added to HEK293T cells expressing human ACE2 for the pseudovirus entry assay. The
392 fitted curves and the 50% neutralizing antibody titers (NT₅₀) were calculated using the
393 Graphpad Prism program. All the measurements were carried out in triplicates.

394 *Western blot*

395 Pseudoviruses were mixed with SDS loading buffer and then were incubated at
396 95°C for 10 min. Samples were run in a 10% SDS Tris-Glycine Gel and transferred to a

397 PVDF membrane. An anti-c9 or anti-His₆ monoclonal primary antibody (1:1000 dilution,
398 Santa Cruz Biotech) and a horseradish peroxidase-conjugated mouse secondary antibody
399 (1:10,000 dilution, Jackson Laboratory) were used for Western blotting. A LAS-4000
400 imager was used to develop images.

401 *Protein pull-down assay*

402 Protein pull-down assay was performed using a Dynabeads immunoprecipitation
403 kit (Invitrogen) as previously described⁴¹. Briefly, 10 µL of Dynabeads, either for His₆-
404 tagged proteins or for Fc-tagged proteins, were washed with PBS buffer and then were
405 incubated with either 8 µg ACE2-His (human ACE2 with a C-terminal His₆ tag) or 10 µg
406 ACE2-Fc (human ACE2 with a C-terminal Fc tag), respectively. Subsequently, ACE2-
407 bound beads were washed with PBS buffer plus 0.05% Tween-20 (PBST) and then were
408 aliquoted into different tubes for later use. To prepare cell-associated coronavirus spike,
409 HEK293T cells were transfected with pcDNA3.1(+) plasmid encoding coronavirus spike
410 (containing a C-terminal c9 tag). 48 h after transfection, the spike-expressing cells were
411 lysed in immunoprecipitation assay buffer using a sonicator and then centrifuged. The
412 supernatants containing solubilized coronavirus spike (or purified recombinant
413 coronavirus RBDs for RBD pull-down assay) were incubated with the ACE2-bound
414 beads (spike or RBD was in excess of ACE2). Then beads were washed with PBST
415 buffer, and the bound proteins were eluted using elution buffer. The samples were then
416 subjected to Western blot analysis and detected using an anti-C9 tag antibody or anti-His₆
417 tag antibody.

418 *Cryo-electron microscopy (cryo-EM)*

419 For sample preparation, aliquots of recombinant SARS-CoV-2 spike ectodomain
420 (3 μ l; 0.35 mg/ml; in buffer containing 10 mM Tris pH7.4 and 100 mM NaCl) were
421 applied to glow-discharged CF-2/1-4C C-flat grids (Protochips). The grids were then
422 plunge-frozen in liquid ethane using a Vitrobot system (FEI Company).

423 For data collection, images were recorded using a Gatan K2 Summit direct
424 electron detector in super resolution mode, attached to a FEI Titan-Krios TEM. The
425 automated software SerialEM was used to collect movies at 22,500x magnification and at
426 a defocus range between 0.6 and 2.6 μ m. 1847 movies were collected for FnM-point
427 spike ectodomain, 4784 movies were collected for FnM-deletion spike ectodomain and
428 4563 movies were collected for K417V/FnM-deletion spike ectodomain. Each movie had
429 an exposure of 7.822 e-/ \AA^2 /s fractionated in 40 frames of 8 second exposure. Data
430 collection statistics are summarized in Table S2.

431 For data processing, whole frames in each movie were corrected for motion and
432 dose compensation using MotionCor2⁴³. The final images were bin-averaged to reach a
433 pixel size of 1.04 \AA . The parameters of the microscope contrast transfer function were
434 estimated for each micrograph using GCTF⁴⁴. Particles were automatically picked and
435 extracted using Gautomatch (<http://www.mrc-lmb.cam.ac.uk/kzhang/Gautomatch/>) and
436 RELION⁴⁵ with a box size of 300 pixels. For FnM-deletion spike ectodomain, 728,804
437 particles were initially extracted and subjected to 2D alignment and clustering using
438 RELION. The best classes were then selected for an additional 2D alignment. ~5,000 best
439 particles were selected for creating the initial 3D model using RELION. 107,268 particles
440 selected from 2D alignment were then subjected to 3D classification. The best class with
441 65,302 particles was subjected to 3D refinement to generate the final density map with

442 C3 symmetry. For FnM-point spike ectodomain, 583,127 particles were initially
443 extracted and subjected to 2D alignment and clustering using RELION. The best classes
444 were then selected for an additional 2D alignment. ~5000 best particles were selected for
445 creating the initial 3D model using RELION. 52,134 particles selected from 2D
446 alignment were then subjected to 3D classification for open and closed conformations.
447 The best open-conformation class with 21,894 particles and the best closed-conformation
448 class with 23,849 particles were subjected to 3D refinement to generate the final density
449 maps with C1 symmetry and C3 symmetry, respectively. For K417V/FnM-deletion spike
450 ectodomain, 1,267,763 particles were initially extracted and subjected to 2D alignment
451 and clustering using RELION. The best classes were then selected for an additional 2D
452 alignment. 124,721 best particles were selected for creating the initial 3D model using
453 RELION. 26,126 particles selected from 2D alignment were then subjected to 3D
454 classification for open and closed conformations. The best open-conformation class with
455 101,413 particles and the best closed-conformation class with 9,502 particles were
456 subjected to 3D refinement to generate the final density maps with C1 symmetry and C3
457 symmetry, respectively. The final density maps were sharpened with modulation transfer
458 function of K2 operated at 300keV using RELION. Reported resolutions were based on
459 the gold standard Fourier shell correlation (FSC) = 0.143 criterion. Fourier shell
460 correction curves were corrected for the effects of soft masking by high-resolution noise
461 substitution ⁴⁶.

462 *Model building and refinement*

463 The initial model of the SARS-CoV-2 spike ectodomain was obtained by fitting
464 the cryo-EM structure of a previously determined SARS-CoV-2 FnM-point spike

465 ectodomain (PDB ID: 6VXX) into our cryo-EM density maps using UCSF Chimera and
466 Coot^{47,48}. Manual model rebuilding was performed using Coot based on the well-defined
467 continuous density of the main chain. Side chain assignments were guided through the
468 density of bulky amino acid residues. The structural model of SARS-CoV-2 spike
469 ectodomain was refined using Phenix⁴⁹ with geometry restraints and three-fold
470 noncrystallographic symmetry constraints. Refinement and model rebuilding were carried
471 out iteratively until no further improvements were achieved in geometry parameters and
472 model-map correlation coefficient. The quality of the final model was analyzed using
473 MolProbity⁵⁰. The validation statistics of the structural models are summarized in Table
474 S2.

475 *Calculation of interface area*

476 The buried surface areas between NTD and RBD and between RBD and RBD in
477 the trimeric spike ectodomains were calculated using the PISA server at the European
478 Bioinformatics Institute (http://www.ebi.ac.uk/pdbe/prot_int/pistart.html)⁵¹. For each
479 trimeric spike ectodomain, a PDB file containing the coordinates from the pair of the
480 corresponding domains was submitted to the PISA server, and the buried surface area for
481 each pair was individually calculated.

482 *Calculation of angle between domains*

483 The rotation angle between the S1 domains in SARS-CoV-2 spike structures was
484 calculated using the angle_between_domains script in the Psico program
485 (<https://pymolwiki.org/index.php/Psico>).

486 *Mouse immunization*

487 Male and female BALB/c mice were intramuscularly (I.M.) immunized with each
488 recombinant SARS-CoV-2 spike ectodomain (10 µg/mouse; 4 mice/group), or PBS
489 buffer, in the presence of two adjuvants: aluminum hydroxide (Alum, 500 µg/mouse;
490 InvivoGen) and monophosphoryl lipid A (MPL, 10 µg/mouse; InvivoGen). The mice
491 were boosted once via I.M. with the same immunogen at 4 weeks. Mouse sera were
492 collected 10 days after the 2nd immunization and detected for antibody responses against
493 the RBD and neutralizing antibodies against SARS-CoV-2 pseudovirus entry.

494 *ELISA*

495 ELISA was carried out to detect the serum IgG antibodies targeting the RBD.
496 Briefly, ELISA plates were coated with recombinant SARS-CoV-2 RBD (containing a C-
497 terminal His tag) (1 µg/ml) at 4°C overnight, and blocked with 2% fat-free milk at 37°C
498 for 2 h. After three washes with wash buffer (PBS + 0.1% Tween-20), the ELISA plates
499 were incubated with each individual mouse serum at serial dilutions. After incubation at
500 37°C for 1 h, the ELISA plates were washed, followed by addition of a horseradish
501 peroxidase-conjugated mouse secondary antibody (1:5,000) (Thermo Fisher Scientific).
502 After another incubation at 37°C for 1 h, ELISA substrate (Sigma-Aldrich) was added.
503 The ELISA reaction was stopped using 1N H₂SO₄, and the ELISA signal was read at the
504 450 nm wavelength using an ELISA plate reader (Tecan).

505 *Ethics statement*

506 Mouse work was performed in strict accordance with the guidance and
507 recommendations in the Guide for the Care and Use of Laboratory Animals (National
508 Research Council Institute for Laboratory Animal Research). Experiments were

509 conducted under animal use protocols approved by the Institutional Animal Care and Use
510 Committees at the New York Blood Center.

511

512

513

514 **References**

- 515 1. Li, Q., *et al.* Early Transmission Dynamics in Wuhan, China, of Novel
516 Coronavirus-Infected Pneumonia. *N Engl J Med* (2020).
- 517 2. Huang, C., *et al.* Clinical features of patients infected with 2019 novel
518 coronavirus in Wuhan, China. *Lancet* (2020).
- 519 3. Lee, N., *et al.* A major outbreak of severe acute respiratory syndrome in Hong
520 Kong. *New England Journal of Medicine* **348**, 1986-1994 (2003).
- 521 4. Peiris, J.S.M., *et al.* Coronavirus as a possible cause of severe acute respiratory
522 syndrome. *Lancet* **361**, 1319-1325 (2003).
- 523 5. Fouchier, R.A.M., *et al.* A previously undescribed coronavirus associated with
524 respiratory disease in humans. *Proceedings of the National Academy of Sciences*
525 *of the United States of America* **101**, 6212-6216 (2004).
- 526 6. van der Hoek, L., *et al.* Identification of a new human coronavirus. *Nature*
527 *Medicine* **10**, 368-373 (2004).
- 528 7. Wu, F., *et al.* Neutralizing antibody responses to SARS-CoV-2 in a COVID-19
529 recovered patient cohort and their implications. *medRxiv*,
530 2020.2003.2030.20047365 (2020).
- 531 8. Zhou, F., *et al.* Clinical course and risk factors for mortality of adult inpatients
532 with COVID-19 in Wuhan, China: a retrospective cohort study. *Lancet* **395**, 1054-
533 1062 (2020).
- 534 9. Woelfel, R., *et al.* Clinical presentation and virological assessment of hospitalized
535 cases of coronavirus disease 2019 in a travel-associated transmission cluster.
536 *medRxiv*, 2020.2003.2005.20030502 (2020).
- 537 10. Gao, M., *et al.* A study on infectivity of asymptomatic SARS-CoV-2 carriers.
538 *Respiratory medicine* **169**, 106026 (2020).
- 539 11. Kronbichler, A., *et al.* Asymptomatic patients as a source of COVID-19
540 infections: A systematic review and meta-analysis. *International journal of*
541 *infectious diseases : IJID : official publication of the International Society for*
542 *Infectious Diseases* **98**, 180-186 (2020).
- 543 12. Graham, R.L. & Baric, R.S. Recombination, reservoirs, and the modular spike:
544 mechanisms of coronavirus cross-species transmission. *J Virol* **84**, 3134-3146
545 (2010).
- 546 13. Li, F. Receptor recognition and cross-species infections of SARS coronavirus.
547 *Antiviral Res* **100**, 246-254 (2013).

- 548 14. Huynh, J., *et al.* Evidence supporting a zoonotic origin of human coronavirus
549 strain NL63. *J Virol* **86**, 12816-12825 (2012).
- 550 15. Ge, X.Y., *et al.* Isolation and characterization of a bat SARS-like coronavirus that
551 uses the ACE2 receptor. *Nature* **503**, 535-538 (2013).
- 552 16. Guan, Y., *et al.* Isolation and characterization of viruses related to the SARS
553 coronavirus from animals in Southern China. *Science* **302**, 276-278 (2003).
- 554 17. Zhou, P., *et al.* A pneumonia outbreak associated with a new coronavirus of
555 probable bat origin. *Nature* (2020).
- 556 18. Li, F. Structure, Function, and Evolution of Coronavirus Spike Proteins. *Annual*
557 *review of virology* **3**, 237-261 (2016).
- 558 19. Du, L.Y., *et al.* The spike protein of SARS-CoV - a target for vaccine and
559 therapeutic development. *Nature Reviews Microbiology* **7**, 226-236 (2009).
- 560 20. Li, F. Receptor recognition mechanisms of coronaviruses: a decade of structural
561 studies. *J Virol* **89**, 1954-1964 (2015).
- 562 21. Belouzard, S., Millet, J.K., Licitra, B.N. & Whittaker, G.R. Mechanisms of
563 coronavirus cell entry mediated by the viral spike protein. *Viruses* **4**, 1011-1033
564 (2012).
- 565 22. Heald-Sargent, T. & Gallagher, T. Ready, set, fuse! The coronavirus spike protein
566 and acquisition of fusion competence. *Viruses* **4**, 557-580 (2012).
- 567 23. Li, W.H., *et al.* Angiotensin-converting enzyme 2 is a functional receptor for the
568 SARS coronavirus. *Nature* **426**, 450-454 (2003).
- 569 24. Wan, Y., Shang, J., Graham, R., Baric, R.S. & Li, F. Receptor Recognition by the
570 Novel Coronavirus from Wuhan: an Analysis Based on Decade-Long Structural
571 Studies of SARS Coronavirus. *J Virol* **94**(2020).
- 572 25. Wu, K., Li, W., Peng, G. & Li, F. Crystal structure of NL63 respiratory
573 coronavirus receptor-binding domain complexed with its human receptor. *Proc*
574 *Natl Acad Sci U S A* **106**, 19970-19974 (2009).
- 575 26. Shang, J., *et al.* Structural basis of receptor recognition by SARS-CoV-2. *Nature*
576 **581**, 221-224 (2020).
- 577 27. Shang, J., *et al.* Cell entry mechanisms of SARS-CoV-2. *Proc Natl Acad Sci U S*
578 *A* **117**, 11727-11734 (2020).
- 579 28. Walls, A.C., *et al.* Structure, Function, and Antigenicity of the SARS-CoV-2
580 Spike Glycoprotein. *Cell* (2020).

- 581 29. Ke, Z., *et al.* Structures and distributions of SARS-CoV-2 spike proteins on intact
582 virions. *Nature* (2020).
- 583 30. Walls, A.C., *et al.* Glycan shield and epitope masking of a coronavirus spike
584 protein observed by cryo-electron microscopy. *Nat Struct Mol Biol* **23**, 899-905
585 (2016).
- 586 31. Wrobel, A.G., *et al.* SARS-CoV-2 and bat RaTG13 spike glycoprotein structures
587 inform on virus evolution and furin-cleavage effects. *Nat Struct Mol Biol* **27**, 763-
588 767 (2020).
- 589 32. Gui, M., *et al.* Cryo-electron microscopy structures of the SARS-CoV spike
590 glycoprotein reveal a prerequisite conformational state for receptor binding. *Cell*
591 *Res* **27**, 119-129 (2017).
- 592 33. Shang, J., *et al.* Structure of mouse coronavirus spike protein complexed with
593 receptor reveals mechanism for viral entry. *PLoS Pathog* **16**, e1008392 (2020).
- 594 34. Xiong, X., *et al.* A thermostable, closed SARS-CoV-2 spike protein trimer. *Nat*
595 *Struct Mol Biol* **27**, 934-941 (2020).
- 596 35. Cai, Y., *et al.* Distinct conformational states of SARS-CoV-2 spike protein.
597 *Science* **369**, 1586-1592 (2020).
- 598 36. Millet, J.K. & Whittaker, G.R. Host cell proteases: Critical determinants of
599 coronavirus tropism and pathogenesis. *Virus Res* **202**, 120-134 (2015).
- 600 37. Yurkovetskiy, L., *et al.* Structural and Functional Analysis of the D614G SARS-
601 CoV-2 Spike Protein Variant. *Cell* **183**, 739-751.e738 (2020).
- 602 38. Ozono, S., *et al.* SARS-CoV-2 D614G spike mutation increases entry efficiency
603 with enhanced ACE2-binding affinity. *Nature communications* **12**, 848 (2021).
- 604 39. Hou, Y.J., *et al.* SARS-CoV-2 D614G variant exhibits efficient replication ex
605 vivo and transmission in vivo. *Science* **370**, 1464-1468 (2020).
- 606 40. Wu, K., *et al.* A Virus-Binding Hot Spot on Human Angiotensin-Converting
607 Enzyme 2 Is Critical for Binding of Two Different Coronaviruses. *Journal of*
608 *Virology* **85**, 5331-5337 (2011).
- 609 41. Wan, Y., *et al.* Molecular Mechanism for Antibody-Dependent Enhancement of
610 Coronavirus Entry. *Journal of Virology* **94**, e02015-02019 (2020).
- 611 42. Peng, G., *et al.* Structural and Molecular Evidence Suggesting Coronavirus-driven
612 Evolution of Mouse Receptor. *J Biol Chem* **292**, 2174-2181 (2017).
- 613 43. Li, X., *et al.* Electron counting and beam-induced motion correction enable near-
614 atomic-resolution single-particle cryo-EM. *Nature methods* **10**, 584-590 (2013).

- 615 44. Zhang, K. Gctf: Real-time CTF determination and correction. *Journal of*
616 *structural biology* **193**, 1-12 (2016).
- 617 45. Scheres, S.H. RELION: implementation of a Bayesian approach to cryo-EM
618 structure determination. *Journal of structural biology* **180**, 519-530 (2012).
- 619 46. Chen, S., *et al.* High-resolution noise substitution to measure overfitting and
620 validate resolution in 3D structure determination by single particle electron
621 cryomicroscopy. *Ultramicroscopy* **135**, 24-35 (2013).
- 622 47. Goddard, T.D., Huang, C.C. & Ferrin, T.E. Visualizing density maps with UCSF
623 Chimera. *Journal of structural biology* **157**, 281-287 (2007).
- 624 48. Emsley, P. & Cowtan, K. Coot: model-building tools for molecular graphics. *Acta*
625 *Crystallographica Section D-Biological Crystallography* **60**, 2126-2132 (2004).
- 626 49. Adams, P.D., *et al.* PHENIX: a comprehensive Python-based system for
627 macromolecular structure solution. *Acta Crystallographica Section D-Biological*
628 *Crystallography* **66**, 213-221 (2010).
- 629 50. Chen, V.B., *et al.* MolProbity: all-atom structure validation for macromolecular
630 crystallography. *Acta crystallographica. Section D, Biological crystallography*
631 **66**, 12-21 (2010).
- 632 51. Krissinel, E. & Henrick, K. Inference of macromolecular assemblies from
633 crystalline state. *J Mol Biol* **372**, 774-797 (2007).
634
- 635

636 **Figure legends:**

637

638 **Figure 1: Molecular switch for SARS-CoV-2 spike to close down.** (A) One-

639 dimensional schematic representation of SARS-CoV-2 spike. NTD: N-terminal domain.

640 RBD: receptor-binding domain. SD1: subdomain 1. SD2: subdomain 2. TM:

641 transmembrane anchor. IC: intracellular tail. Furin cleavage site is indicated by arrow.

642 (B) Three-dimensional schematic representation of SARS-CoV-2 spike in the pre-fusion

643 structure. The double curve arrow indicates a mixture of open and closed spikes. Double

644 dotted lines represent viral envelope. Arrows indicate location of furin motif (FnM). Also

645 listed is the comparison of the sequences in the furin motif region among SARS-CoV-2,

646 RaTG13-CoV and SARS-CoV-1 spikes. SARS-CoV-2 (FnM-point) spike contains point

647 mutations in FnM. SARS-CoV-2 (FnM-deletion) spike contains FnM deletion as in

648 SARS-CoV-1. SARS-CoV-2 (FnM-deletion-2) spike contains FnM deletion as in

649 RaTG13-CoV. (C) Protein pull-down assay using recombinant human ACE2 as the bait

650 and cell-associated SARS-CoV-2 spike molecules (wild type and mutants) as the targets.

651 Protein levels were detected using Western blot. Top, cell-expressed SARS-CoV-2 spike.

652 Middle, pull-down results using His₆-tagged ACE2. Bottom, pull-down results using Fc-

653 tagged ACE2. The expression of SARS-CoV-2 spike (which contained a C-terminal c9

654 tag) was detected using an anti-c9 antibody. Mock, no spike. WT, wild type. (D) SARS-

655 CoV-2 pseudovirus entry into human ACE2-expressing cells. Top, pseudovirus entry

656 efficiency normalized against the expression of the spike (see bottom). Entry efficiency

657 of wild type pseudoviruses was taken as 100%. Bottom, SARS-CoV-2 spike (which

658 contained a C-terminal c9 tag) packaged in pseudoviruses. Its expression was detected by

659 Western blot using an anti-c9 antibody. Individual data points are shown as dots. A

660 comparison (two-tailed Student's t-test) was performed on data between different groups
661 (n=8). ***P < 0.001. All experiments were repeated independently three times with
662 similar results.

663

664 **Figure 2: Cryo-EM analyses of the conformations of recombinant SARS-CoV-2**
665 **spike ectodomain mutants.** These spike mutants contain furin motif deletion (A), furin
666 motif point mutations (B), or both K17V mutation and furin motif deletion (C),
667 respectively. Details of these mutations were explained in Fig. 1B. Their EM density
668 maps, corresponding resolution, and distribution of the particles in open and closed
669 conformations are shown. Atomic models were built for the closed spikes containing
670 furin motif deletion and furin motif point mutations, respectively. Three-dimensional
671 schematic representations are shown for the other spike particles.

672

673 **Figure 3: Molecular switch for RaTG13-CoV spike to open up.** (A) Three-
674 dimensional schematic representation of RaTG13-CoV spike in the pre-fusion structure
675 with closed RBDs. RaTG13-CoV (FnM-insert) spike contains inserted FnM as in SARS-
676 CoV-2. RaTG13-CoV (GSGS-insert) spike contains an inserted GSGS sequence in the
677 same location as FnM. (B) Protein pull-down assay using recombinant human ACE2 as
678 the bait and cell-associated RaTG13-CoV spike molecules as the targets. Top, cell-
679 expressed RaTG13-CoV spike. Middle, pull-down results using His₆-tagged ACE2.
680 Bottom, pull-down results using Fc-tagged ACE2. (C) RaTG13-CoV pseudovirus entry
681 into human ACE2-expressing cells. Top, pseudovirus entry efficiency normalized against
682 the expression level of the spike (see bottom). Bottom, RaTG13-CoV spike packaged in

683 pseudoviruses. Data are mean + S.E.M. A comparison (two-tailed Student's t-test) was
684 performed on data between different groups (n=4). ***P < 0.001. All experiments were
685 repeated independently three times with similar results.

686

687 **Figure 4: Molecular switch for SARS-CoV-2 spike to open up.** (A) Identification of a
688 critical residue Lys417 in SARS-CoV-2 spike that stabilizes the RBD in the closed
689 conformation. The corresponding residue is a valine in SARS-CoV-1. The structure of
690 the closed SARS-CoV-2 spike (PDB 6VXX) is presented from a side view to show three
691 packed RBDs. Each monomeric subunit of the spike trimer is colored differently. (B)
692 Protein pull-down assay using recombinant human ACE2 as the bait and cell-associated
693 SARS-CoV-2 spike molecules as the targets. Top, cell-expressed SARS-CoV-2 spike.
694 Middle, pull-down results using His₆-tagged ACE2. Bottom, pull-down results using Fc-
695 tagged ACE2. (C) SARS-CoV-2 pseudovirus entry into human ACE2-expressing cells.
696 Top, pseudovirus entry efficiency normalized against the expression level of the spike
697 (see bottom). Bottom, SARS-CoV-2 spike in packaged pseudoviruses. Data are mean +
698 S.E.M. A comparison (two-tailed Student's t-test) was performed on data between
699 different groups (n=8). ***P < 0.001. All experiments were repeated independently three
700 times with similar results.

701

702 **Figure 5: Immune evasion of closed SARS-CoV-2 spike.** Mice were immunized with
703 one of the mutant SARS-CoV-2 spikes (4 mice in each group). Subsequently the mouse
704 sera were assayed for titers of RBD-targeting antibodies and neutralizing antibodies.
705 Buffer PBS was used as a negative control in mouse immunization. (A) ELISA for

706 detecting the titers of RBD-targeting IgG antibodies. SARS-CoV-2 RBD (containing a C-
707 terminal His₆ tag) was coated on ELISA plates, and serially diluted sera from each
708 immunized mouse were added for detection of RBD/IgG binding. The titers were
709 expressed as the endpoint dilutions that remain positively detectable. A titer was
710 determined for sera from each immunized mouse. Data are mean + S.E.M. A comparison
711 (two-tailed Student's t-test) was performed on sera between the FnM-deletion group and
712 one of the other experimental mouse groups (n=4). ***P < 0.01. *P < 0.05. (B)

713 Pseudovirus entry inhibition assay for detecting the titers of neutralizing antibodies.
714 SARS-CoV-2 pseudoviruses were used to enter human ACE2-expressing cells in the
715 presence of serially diluted sera from each group of immunized mice (sera from mice
716 within each immunization group were pooled together for this assay). NT₅₀ of sera was
717 determined as the dilution factor that led to 50% inhibition of pseudovirus entry. High
718 NT₅₀ suggests high titers of neutralizing antibodies in the sera. Data are mean + S.E.M.
719 A comparison (two-tailed Student's t-test) was performed on sera at individual dilution
720 point between the FnM-deletion group and one of the other experimental mouse groups
721 (n=3). ***P < 0.001. **P < 0.01. *P < 0.05. All experiments were repeated independently
722 three times with similar results.

723

724

725 **Supplementary figure legends**

726 **Figure S1: Cryo-EM classifications of SARS-CoV-2 spike particles. (A)**

727 Representative 2D class averages in different orientations. (B) Summary of 3D
728 classifications of SARS-CoV-2 spike particles.

729

730 **Figure S2: Cryo-EM data for two mutant SARS-CoV-2 spikes whose atomic models**

731 **were built.** (A) Gold-standard Fourier shell correlation (FSC) curves. The resolutions

732 were set at 3.8 Å for FnM-deletion spike and 4.37 Å for FnM-point spike. The 0.143

733 cutoff value is indicated by horizontal dotted line. (B) Partial cryo-EM density maps with

734 fitted atomic models for FnM-deletion spike (model in blue) and for FnM-point spike

735 (model in red).

736

737 **Figure S3: S1 packing in SARS-CoV-2 spike. (A)** Structure of trimeric S1 in FnM-

738 deletion spike. Three subunits are colored differently. Noted in parentheses are the

739 monomeric subunits where each structural element is located. (B) Comparison of S1

740 packing in two cryo-EM structures determined in the current study (FnM-deletion spike

741 in the closed conformation and FnM-point spike in the closed conformation) and another

742 cryo-EM structure determined in a previous study (FnM-point spike in the closed

743 conformation; PDB: 6VXX).

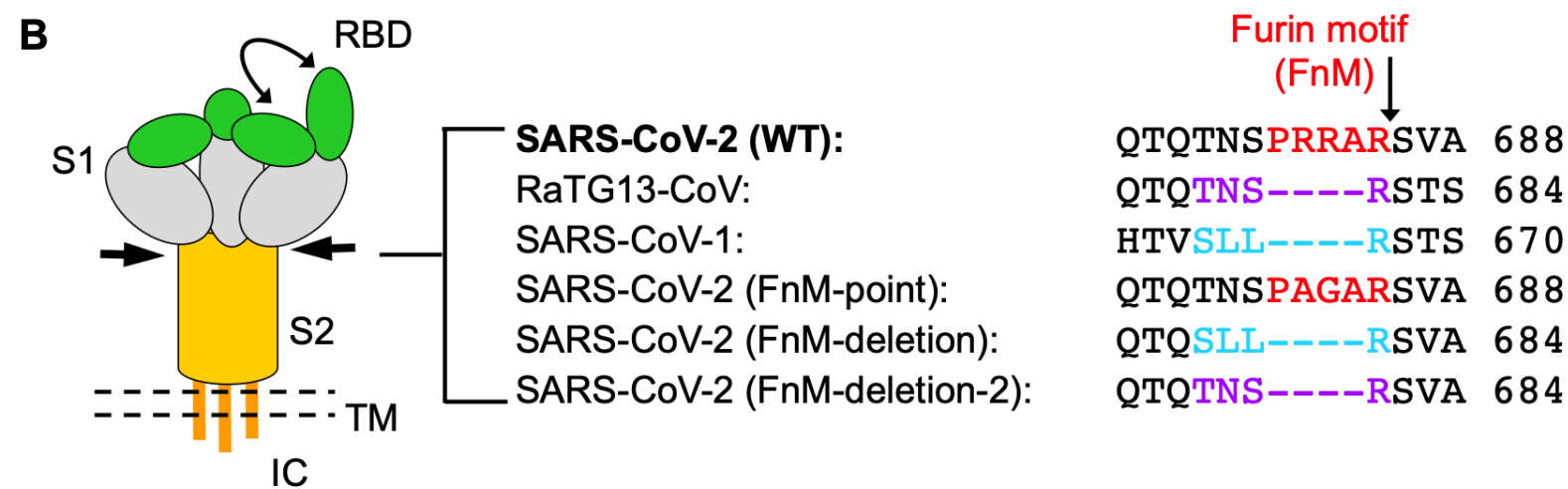
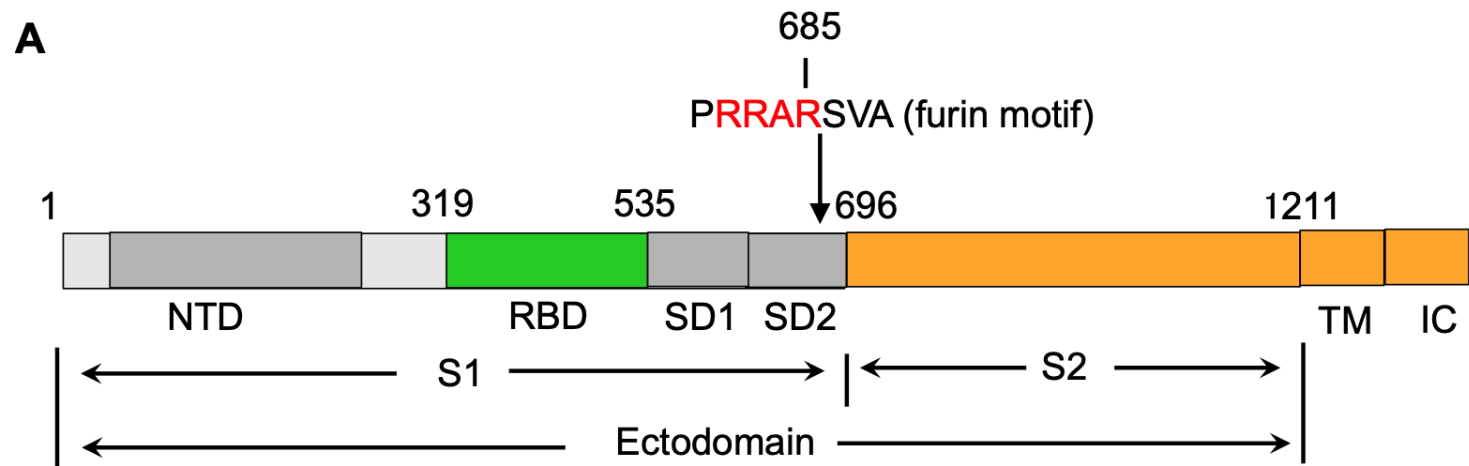
744

745 **Figure S4: Role of furin motif loop in S1 packing (A)** Comparison of chain traces of

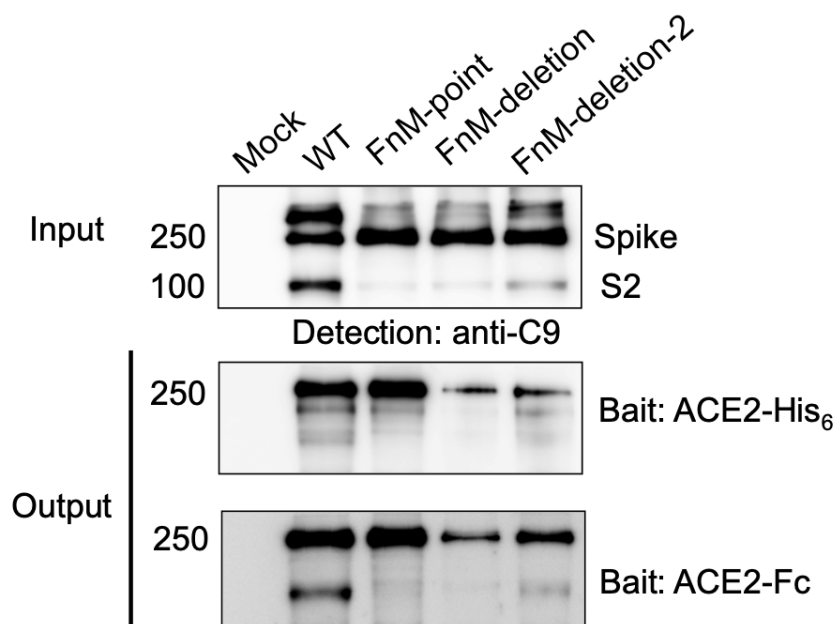
746 monomeric S1 in FnM-deletion spike (colored in blue) and that in FnM-point spike

747 (colored in red). (B) Comparison of chain traces of monomeric S1 in FnM-deletion spike

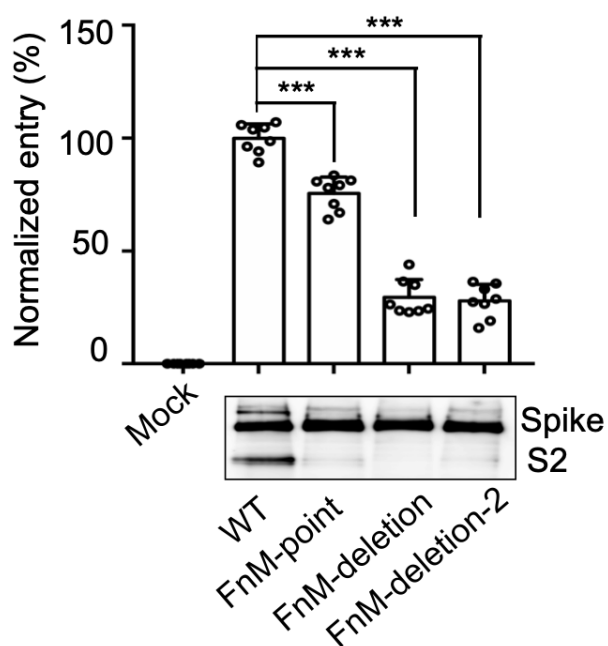
748 (colored in red) and that in mouse hepatitis coronavirus (MHV) spike (colored in red;
749 PDB: 6VSJ).



C
Pull down of cell-surface SARS-CoV-2 spike



D
SARS-CoV-2 pseudovirus



A Furin motif deletion

3.8 Å



Closed (100%)

RBD



B Furin motif point mutations

4.4 Å



Closed (52%)

RBD

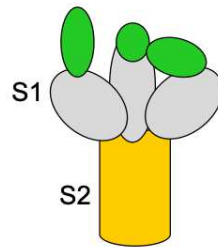


5.3 Å



Open (48%)

RBD



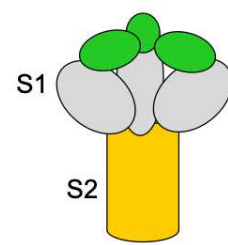
C RBD mutation (K417V)
+ Furin motif deletion

4.6 Å



Closed (9%)

RBD

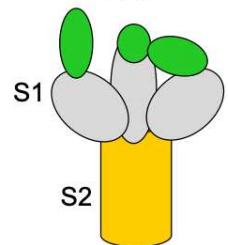


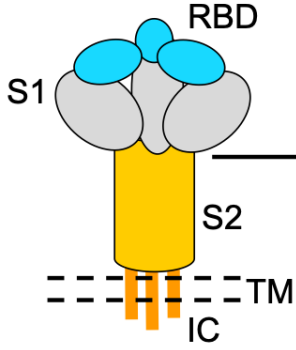
4.6 Å



Open (91%)

RBD



A

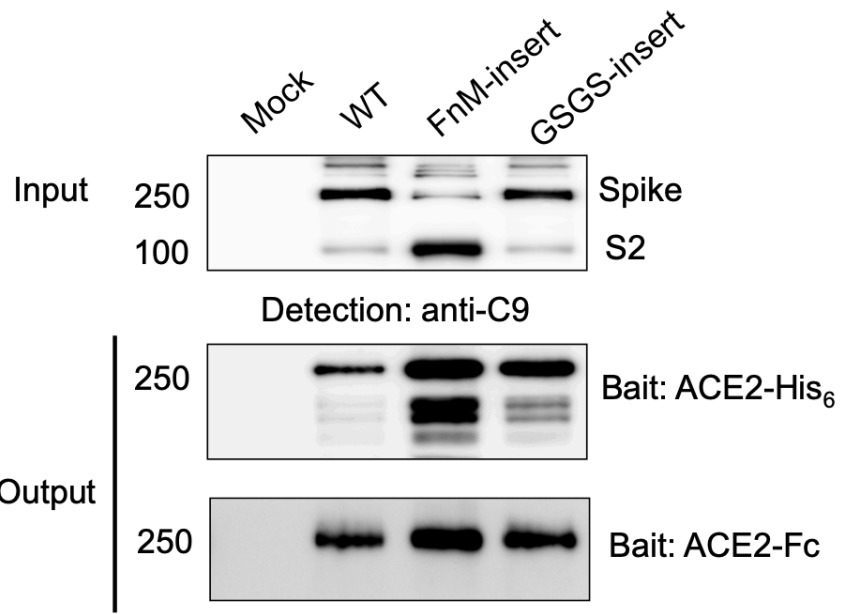
RaTG13-CoV (WT):
SARS-CoV-2:
RaTG13-CoV (FnM-insert):
RaTG13-CoV (GSGS-insert):

Furin motif (FnM)

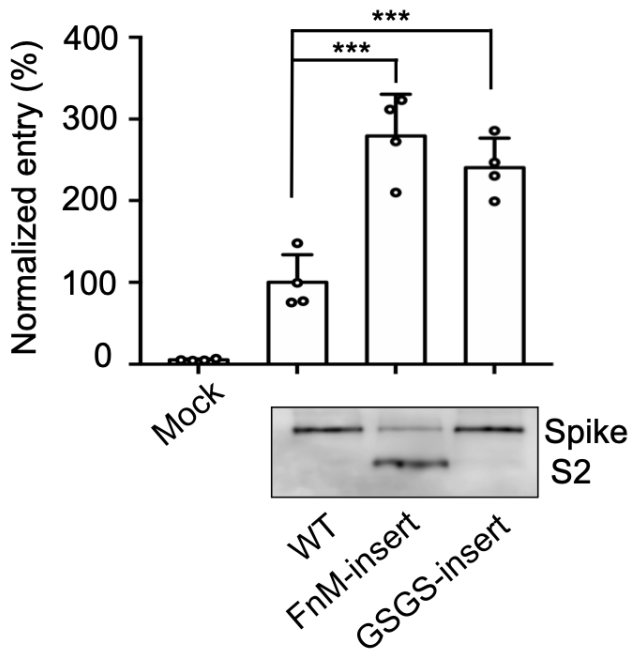
QTQ**TNS**----RSTS 684
 QTQ**TNSPRRARSVA** 688
 QTQ**TNSPRRAR**STS 688
 QTQ**TNSGSGSR**STS 688

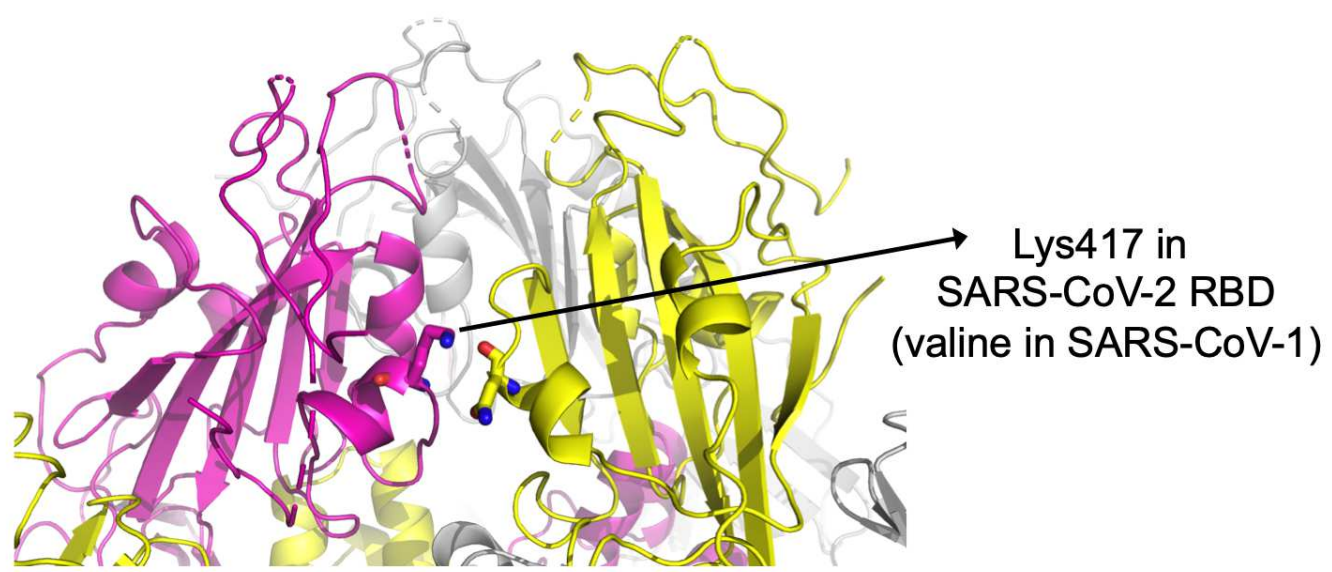
B

Pull down of cell-surface RaTG13-CoV spike

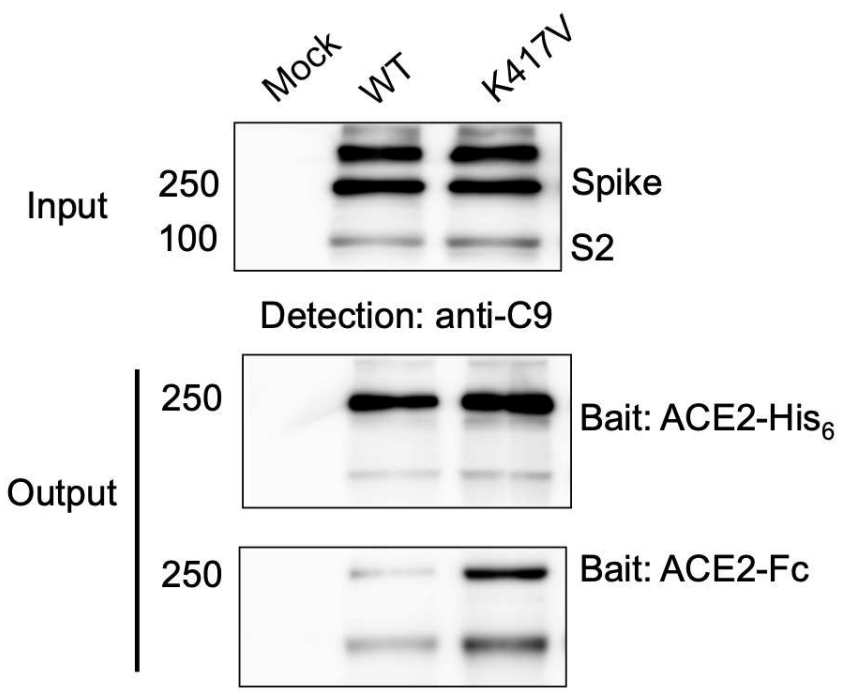
**C**

RaTG13-CoV pseudovirus

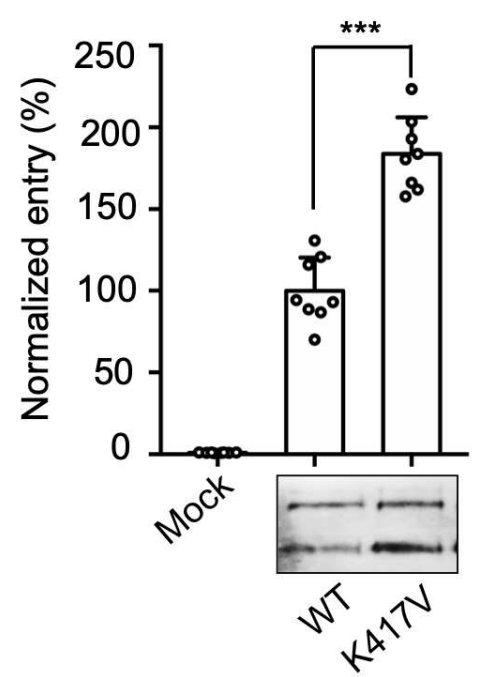


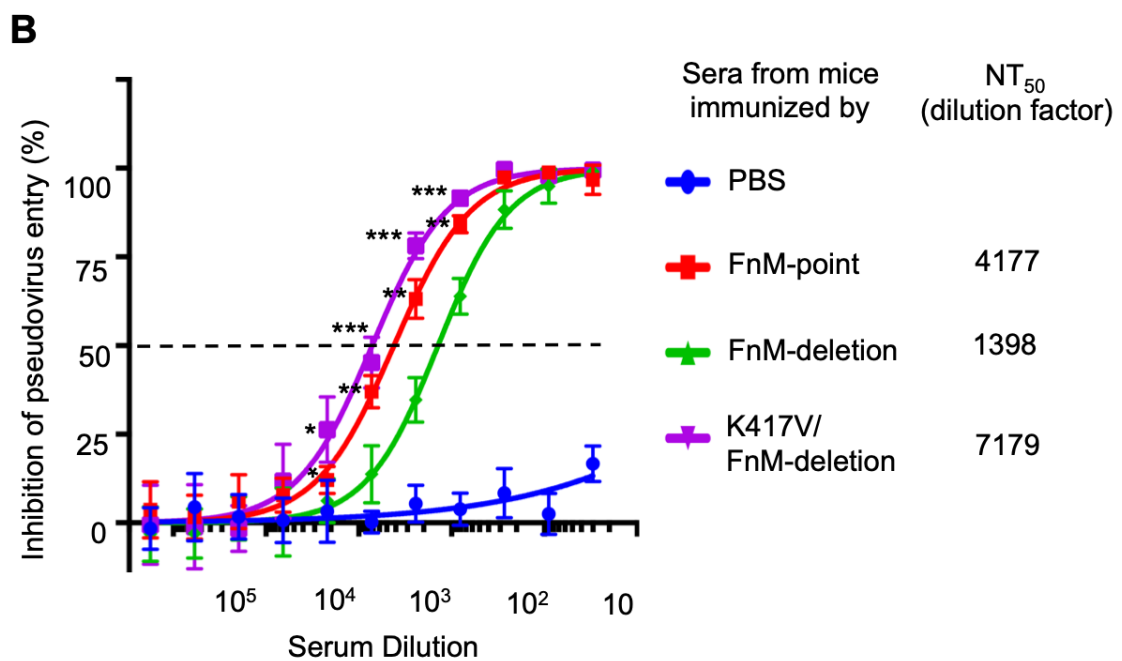
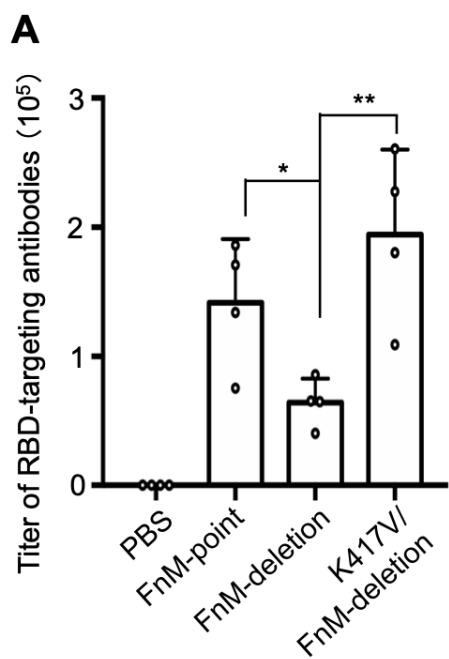
A**B**

Pull down of cell-surface SARS-CoV-2 spike

**C**

SARS-CoV-2 pseudovirus





Figures

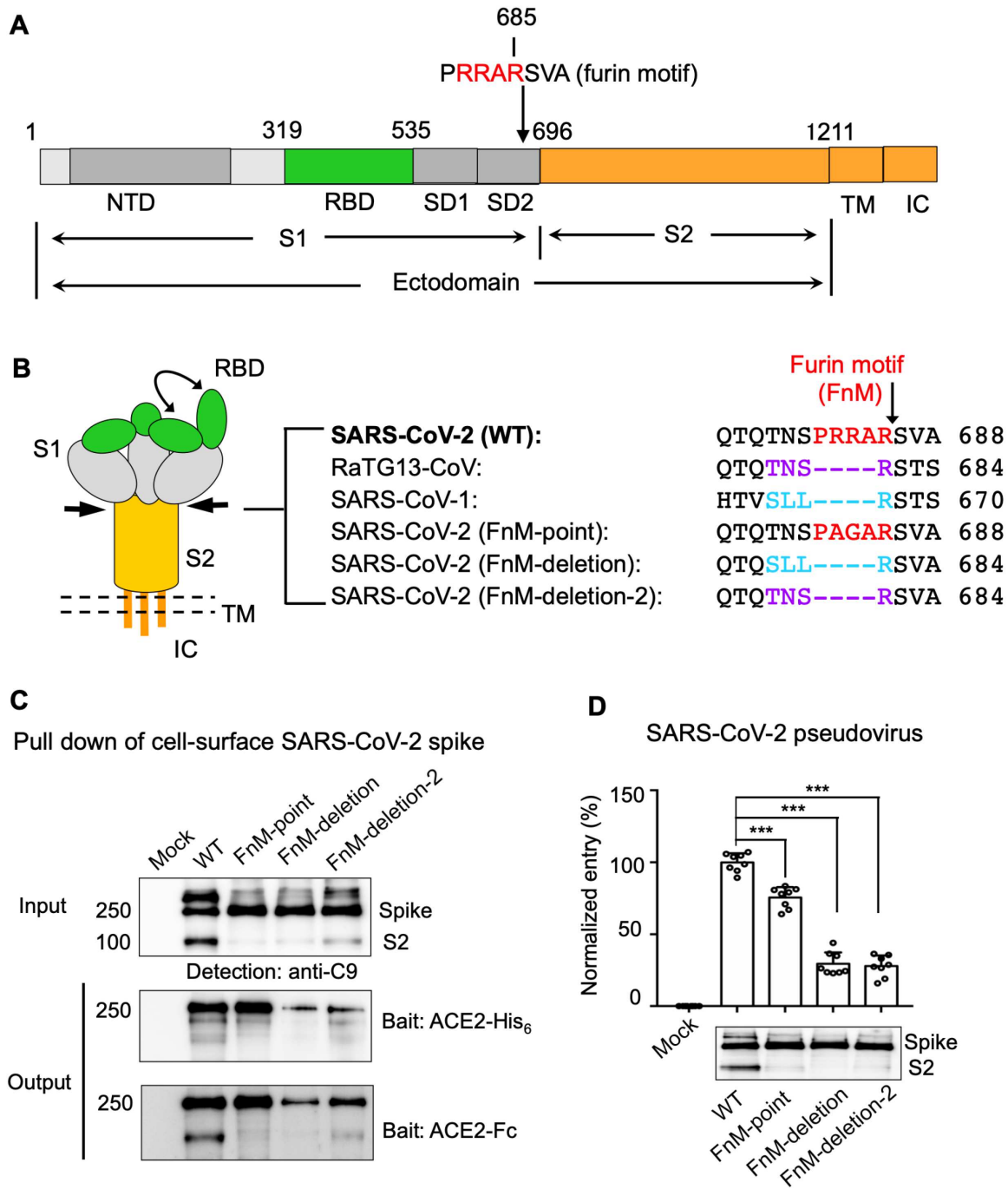


Figure 1

Molecular switch for SARS-CoV-2 spike to close down. (A) One-dimensional schematic representation of SARS-CoV-2 spike. NTD: N-terminal domain. RBD: receptor-binding domain. SD1: subdomain 1. SD2: subdomain 2. TM: transmembrane anchor. IC: intracellular tail. Furin cleavage site is indicated by arrow.

(B) Three-dimensional schematic representation of SARS-CoV-2 spike in the pre-fusion structure. The double curve arrow indicates a mixture of open and closed spikes. Double dotted lines represent viral envelope. Arrows indicate location of furin motif (FnM). Also listed is the comparison of the sequences in the furin motif region among SARS-CoV-2, RaTG13-CoV and SARS-CoV-1 spikes. SARS-CoV-2 (FnM-point) spike contains point mutations in FnM. SARS-CoV-2 (FnM-deletion) spike contains FnM deletion as in SARS-CoV-1. SARS-CoV-2 (FnM-deletion-2) spike contains FnM deletion as in RaTG13-CoV. (C) Protein pull-down assay using recombinant human ACE2 as the bait and cell-associated SARS-CoV-2 spike molecules (wild type and mutants) as the targets. Protein levels were detected using Western blot. Top, cell-expressed SARS-CoV-2 spike. Middle, pull-down results using His 6 -tagged ACE2. Bottom, pull-down results using Fc- tagged ACE2. The expression of SARS-CoV-2 spike (which contained a C-terminal c9 tag) was detected using an anti-c9 antibody. Mock, no spike. WT, wild type. (D) SARS-CoV-2 pseudovirus entry into human ACE2-expressing cells. Top, pseudovirus entry efficiency normalized against the expression of the spike (see bottom). Entry efficiency of wild type pseudoviruses was taken as 100%. Bottom, SARS-CoV-2 spike (which contained a C-terminal c9 tag) packaged in pseudoviruses. Its expression was detected by Western blot using an anti-c9 antibody. Individual data points are shown as dots. A comparison (two-tailed Student's t-test) was performed on data between different groups (n=8). ***P < 0.001. All experiments were repeated independently three times with similar results.

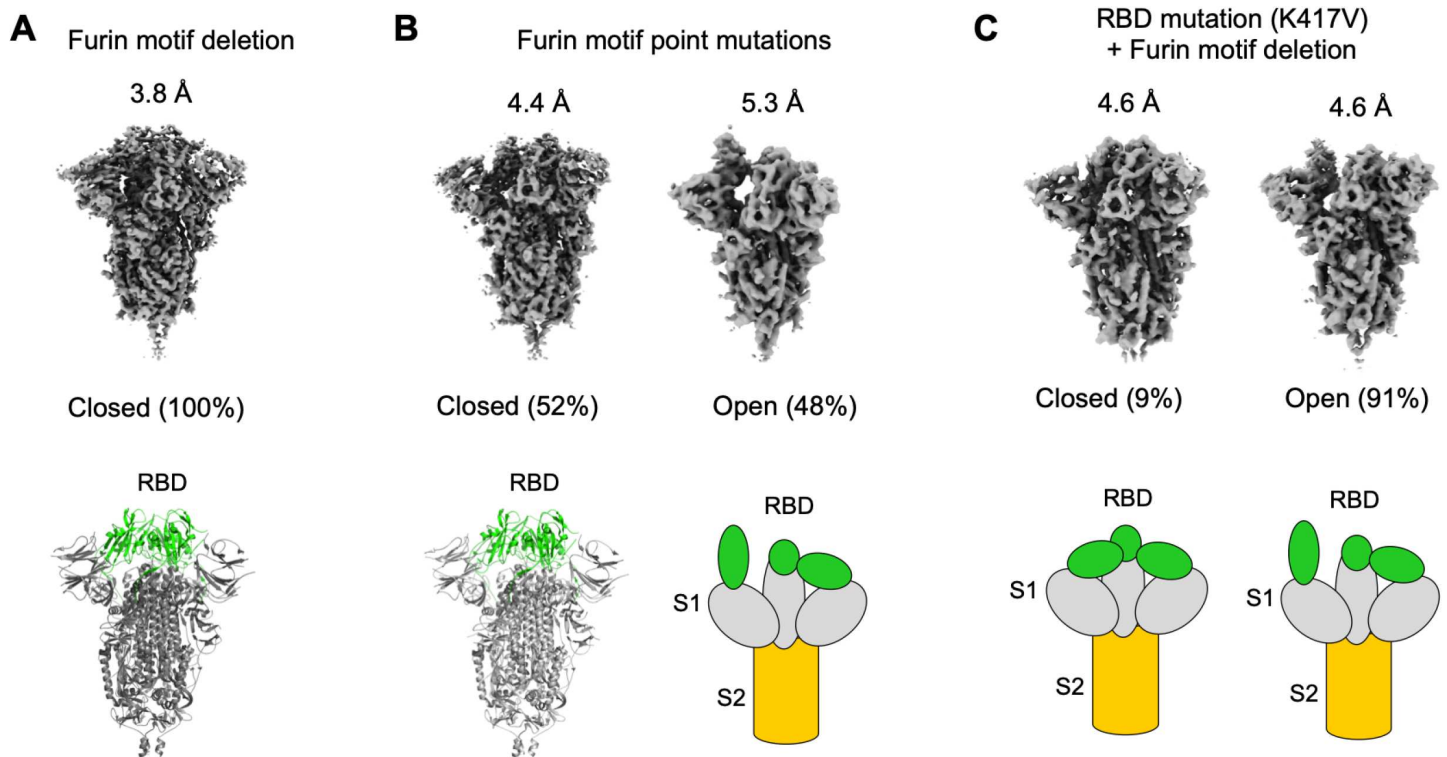


Figure 2

Cryo-EM analyses of the conformations of recombinant SARS-CoV-2 spike ectodomain mutants. These spike mutants contain furin motif deletion (A), furin motif point mutations (B), or both K17V mutation and furin motif deletion (C), respectively. Details of these mutations were explained in Fig. 1B. Their EM

density maps, corresponding resolution, and distribution of the particles in open and closed conformations are shown. Atomic models were built for the closed spikes containing furin motif deletion and furin motif point mutations, respectively. Three-dimensional schematic representations are shown for the other spike particles.

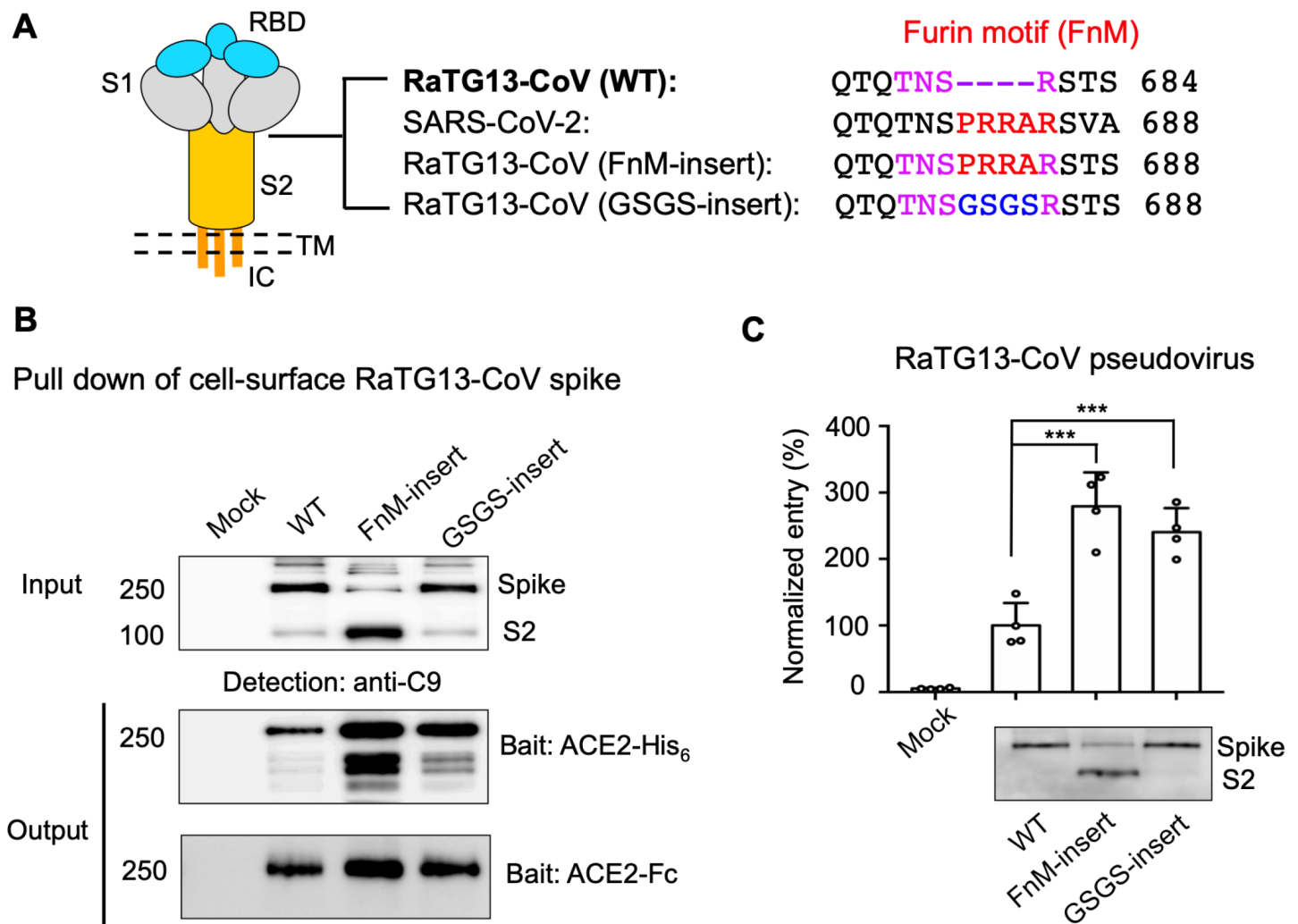


Figure 3

Molecular switch for RaTG13-CoV spike to open up. (A) Three-dimensional schematic representation of RaTG13-CoV spike in the pre-fusion structure with closed RBDs. RaTG13-CoV (FnM-insert) spike contains inserted FnM as in SARS-CoV-2. RaTG13-CoV (GSGS-insert) spike contains an inserted GSGS sequence in the same location as FnM. (B) Protein pull-down assay using recombinant human ACE2 as the bait and cell-associated RaTG13-CoV spike molecules as the targets. Top, cell-expressed RaTG13-CoV spike. Middle, pull-down results using His₆-tagged ACE2. Bottom, pull-down results using Fc-tagged ACE2. (C) RaTG13-CoV pseudovirus entry into human ACE2-expressing cells. Top, pseudovirus entry efficiency normalized against the expression level of the spike (see bottom). Bottom, RaTG13-CoV spike packaged in pseudoviruses. Data are mean + S.E.M. A comparison (two-tailed Student's t-test) was performed on data between different groups (n=4). ***P < 0.001. All experiments were repeated independently three times with similar results.

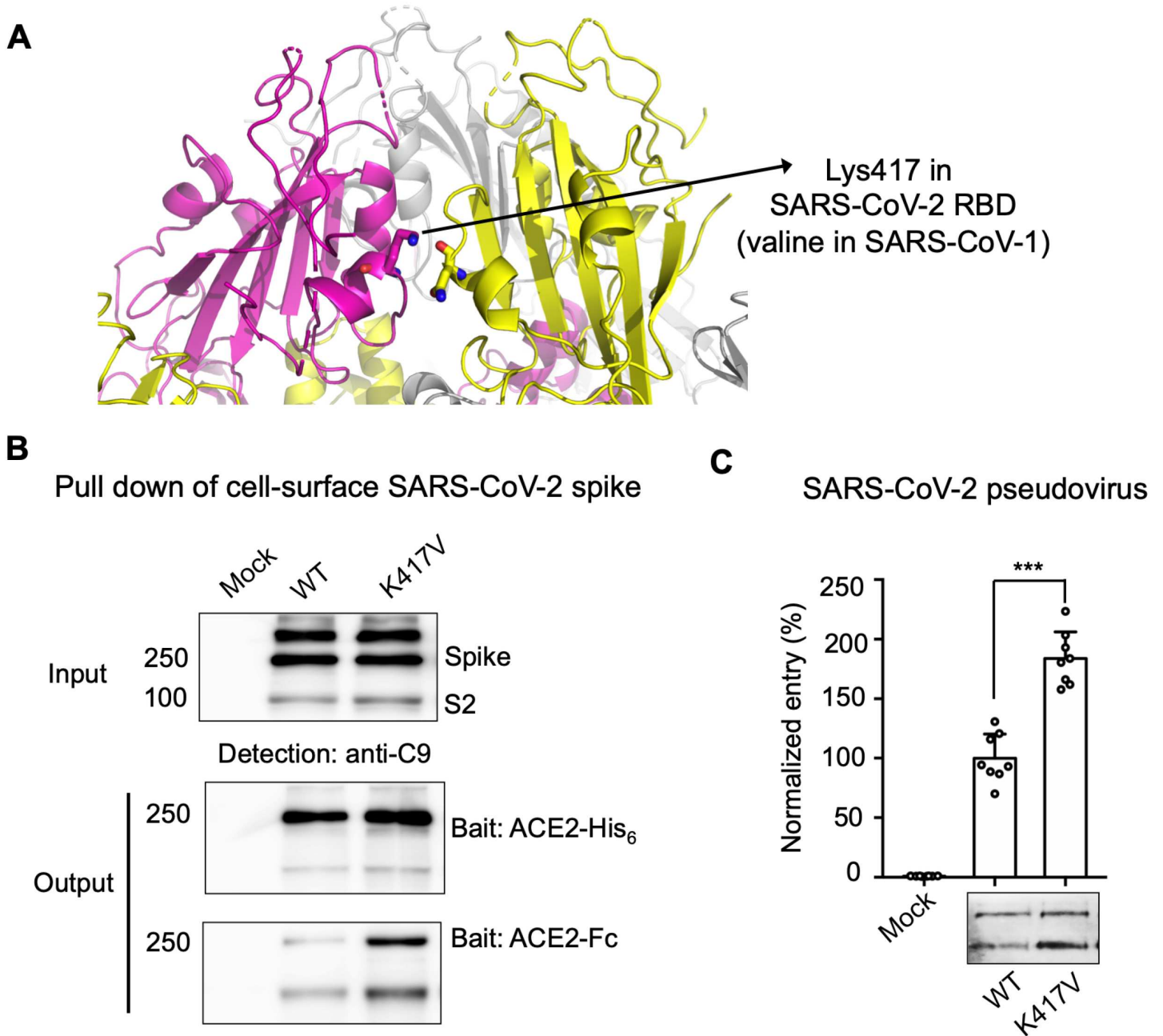


Figure 4

Molecular switch for SARS-CoV-2 spike to open up. (A) Identification of a critical residue Lys417 in SARS-CoV-2 spike that stabilizes the RBD in the closed conformation. The corresponding residue is a valine in SARS-CoV-1. The structure of the closed SARS-CoV-2 spike (PDB 6VXX) is presented from a side view to show three packed RBDs. Each monomeric subunit of the spike trimer is colored differently. (B) Protein pull-down assay using recombinant human ACE2 as the bait and cell-associated SARS-CoV-2 spike molecules as the targets. Top, cell-expressed SARS-CoV-2 spike. Middle, pull-down results using His 6 - tagged ACE2. Bottom, pull-down results using Fc- tagged ACE2. (C) SARS-CoV-2 pseudovirus entry into human ACE2-expressing cells. Top, pseudovirus entry efficiency normalized against the expression level of the spike (see bottom). Bottom, SARS-CoV-2 spike in packaged pseudoviruses. Data are mean + S.E.M.

A comparison (two-tailed Student's t-test) was performed on data between different groups (n=8). ***P < 0.001. All experiments were repeated independently three times with similar results.

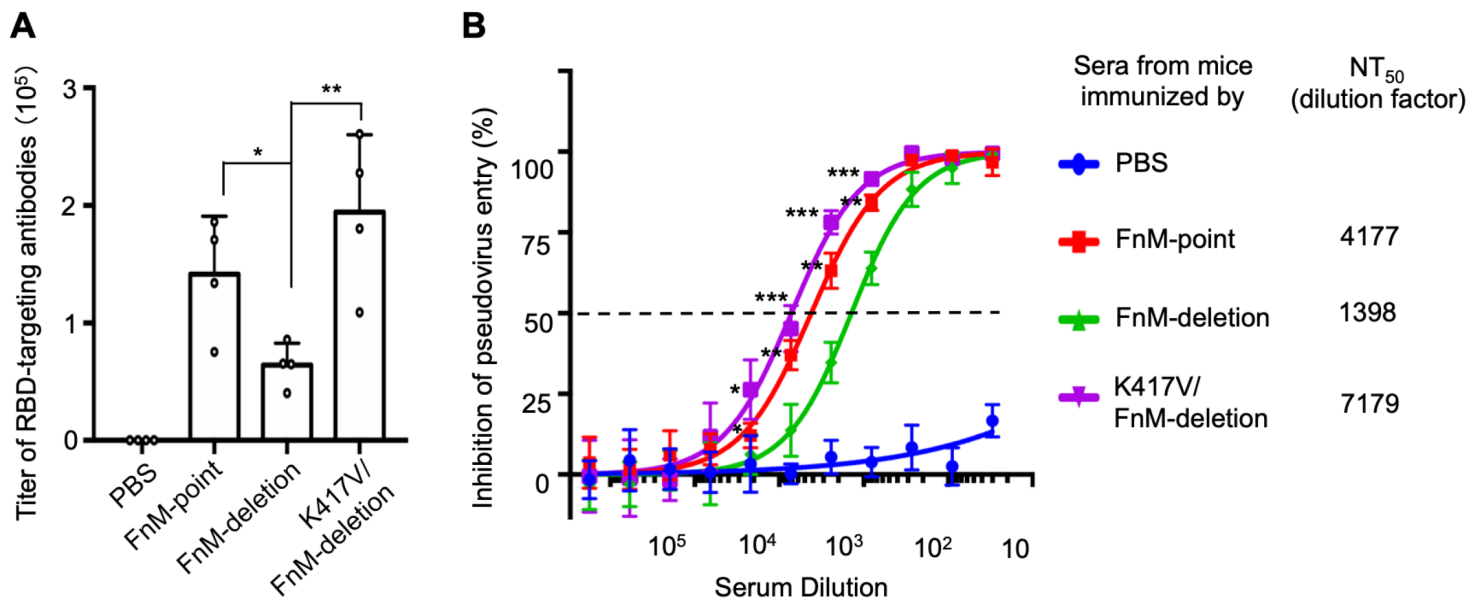


Figure 5

Immune evasion of closed SARS-CoV-2 spike. Mice were immunized with one of the mutant SARS-CoV-2 spikes (4 mice in each group). Subsequently the mouse sera were assayed for titers of RBD-targeting antibodies and neutralizing antibodies. Buffer PBS was used as a negative control in mouse immunization. (A) ELISA for detecting the titers of RBD-targeting IgG antibodies. SARS-CoV-2 RBD (containing a C-terminal His 6 tag) was coated on ELISA plates, and serially diluted sera from each immunized mouse were added for detection of RBD/IgG binding. The titers were expressed as the endpoint dilutions that remain positively detectable. A titer was determined for sera from each immunized mouse. Data are mean + S.E.M. A comparison (two-tailed Student's t-test) was performed on sera between the FnM-deletion group and one of the other experimental mouse groups (n=4). **P < 0.01. *P < 0.05. (B) Pseudovirus entry inhibition assay for detecting the titers of neutralizing antibodies. SARS-CoV-2 pseudoviruses were used to enter human ACE2-expressing cells in the presence of serially diluted sera from each group of immunized mice (sera from mice within each immunization group were pooled together for this assay). NT 50 of sera was determined as the dilution factor that led to 50% inhibition of pseudovirus entry. High NT 50 suggests high titers of neutralizing antibodies in the sera. Data are mean + S.E.M. A comparison (two-tailed Student's t-test) was performed on sera at individual dilution point between the FnM-deletion group and one of the other experimental mouse groups (n=3). ***P < 0.001. **P < 0.01. *P < 0.05. All experiments were repeated independently three times with similar results.

Supplementary Files

This is a list of supplementary files associated with this preprint. Click to download.

- [175810supp194363qvr5lcconvrt.pdf](#)